JMU

JOHANNES KEPLER
UNIVERSITY LINZ

Optical and electrochemical band gap determination of lead halide perovskites in a band gap range from 1.5 eV to 2.5 eV
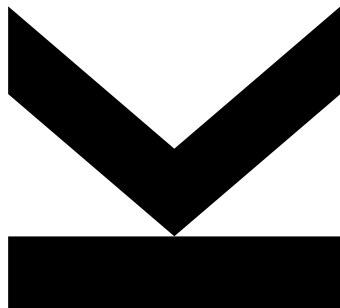
Author
Rene Zahrhuber

Submission
Institute of Physical Chemistry and Linz Institute for Organic Solar Cells

Thesis Supervisor
Assoc. Prof. DI Dr. Markus Scharber

Co-Supervisor
DI Katarina Gugujonovic

September 2022

Bachelor Thesis

to confer the academic degree of

Bachelor of Science (BSc)

in the Bachelor's Program

Chemistry and Chemical Technology

Acknowledgment

Abstract

Lead halide perovskite solar cells have gained tremendous interest over the past decades. Their low production costs and outstanding properties turn them into competitive alternatives to their commercially well-established silicon counterparts. Fields of application are the use in tandem solar cells and LEDs. In order to obtain the best working conditions in such devices, band gap tuning of the lead halide perovskite is performed. This can be realized by modification upon the X-sited anions in the lead halide perovskite structure. However, wide band gap perovskite solar cells typically suffer from a high loss in open circuit voltage (V_{OC}). One main challenge to reduce the open circuit voltage loss ($V_{OC, loss}$) is to find suitable materials that are capable for the use as interlayer. In this thesis, several lead halide perovskite compositions were tested in solar cells with p-i-n configuration. The band gap of the perovskites is determined optically and electrochemically and compared with the performance of the devices. Besides varying the halide content, a new hole transport material (MeO-2PACz) is also investigated. As HTMs are one of the most expensive components of perovskite solar cells, there is a major interest in finding cheap and good working materials.

Kurzfassung

Das Interesse an Blei-Halogenid Perowskit Solarzellen ist über die letzten Jahrzehnte enorm angestiegen. Nicht nur die geringen Produktionskosten, sondern auch deren herausragenden Eigenschaften machen sie zu konkurrenzfähigen alternativen gegenüber den wirtschaftlich bewährten Silizium Solarzellen. Einsatz finden Blei-Halogenid Perowskit Solarzellen in Tandem Solarzellen sowie in LEDs. Um geeignete Betriebsparameter in jenen Bauteilen zu gewährleisten, muss die Bandlücke im Perowskit verändert werden. Dies kann zum Beispiel über den Austausch eines Anions an Position X in der Kristallgitterstruktur umgesetzt werden. Typischerweise sind Perowskit Solarzellen mit großen Bandlücken von hohen Klemmenspannungs-Verlusten betroffen. Ein Hauptaugenmerk hierbei ist es geeignete Materialien für Zwischenschichten zu finden um den Klemmenspannungsverlust zu veringern. Im Rahmen dieser Arbeit wurden verschiedene Zusammensetzungen von Blei-Halogenid Perowskit Solarzellen in p-i-n Konfiguration getestet. Die Bandlücke der Perowskite wird optisch und elektrochemisch bestimmt, und mit der Performance der Solarzellen verglichen. Neben den veränderten Halogenidanteilen, wurden ebenso neue Lochleitermaterialien (MeO-2PACz) getestet. Da Lochleitermaterialien eine der teuersten Komponenten in der Herstellung von Perowskitsolarzellen sind, besteht ein großes Interesse daran günstige und gut funktionierende Alternativen zu finden.

Contents

1 Introduction

Over the past decade, organic-inorganic halide perovskites (OIHP) have received more and more attention due to their outstanding electrical and optical properties. OIHPs are generally represented as ABX_3, where A is a methylammonium (CH_3NH_3) ion or formamidinium ($NH=CHNH_3$) ion, B is a Pb, Sn, Cs, or Cd ion, and X is occupied by a halogen ion, like I⁻, Br⁻, or Cl⁻ [1]. Due to the crystal structure, electron and hole transport mechanisms are improved in perovskites. A change in optoelectronic properties can be achieved upon modification of the different precursor solutions. Changing the X-sited anion affects the band gap, trap density states, and the crystal structure. At the same time, increasing the concentration of the precursor solution leads to an increase in grain size [2, 3]. Hole transport materials (HTMs) are one important constituent in perovskite solar cells (PSCs). Similar or equal ionization potentials of the hole transport materials and the perovskite layers are important for the selection. Depending on the desired properties, inorganic and organic hole transport materials are available. Especially the probability of non-radiative recombination can decrease by choosing a proper HTM, which results in higher open-circuit voltages [1, 4]. In general, the optoelectronic properties of OIHPs strongly depend on the semiconductor band gap. Therefore, fast and safe determination methods are necessary. Recording the absorption coefficient α or the external quantum efficiency (EQE) and plotting them in a Tauc plot, is a frequently used method [5]. Electrochemistry is another method to determine the band gaps (valence band (VB) and conduction band (CB)) of perovskite films. Cyclic voltammetry (CV) and electrochemical voltage spectroscopy (EVS) are two common electroanalytical techniques for this issue. In contrast to optical determination, electrochemistry is a fast determination method and light scattering within the perovskite (due to opaque layers) does not play a role. One disadvantage of the electrochemical method is the instability of the perovskite films to the used solvents and experimental conditions [6].

1.1 Crystal structure and morphology

Organic-inorganic halide perovskites can be described by a general formula ABX_3. These materials have high absorption coefficients, a low exciton binding energy (2 meV) and a direct band gap. Also, their high charge carrier mobility (diffusion lengths of a few microns) makes them ideal photovoltaic materials [1]. The band gap, one key requirement for photovoltaic applications, can easily be varied by the partially changing the X-sited anion. Substitution of the I- ion for a Br- ion, for example, increases the bandgap. Also, the change in the organic cation leads to similar results.

Changing the ionic radii of the atoms leads to a change in the symmetry of the perovskite structure. The crystal structure of ABX_3 (see Fig. 1) can be described by the perovskite tolerance factor (t), also called Goldschmidt factor.

$$t = \frac{r_A + r_X}{\sqrt{2}(r_B + r_X)} \; ,$$

(1)

In Eq. 1, r_A, r_B, r_X are the ionic radii of the respective perovskite ions. For example, replacing the methylammonium ion with a formamidinium ion increase the tolerance factor. Thereby, the symmetry of the crystal structure is increased, resulting in a reduction in the electronic band gap [2].
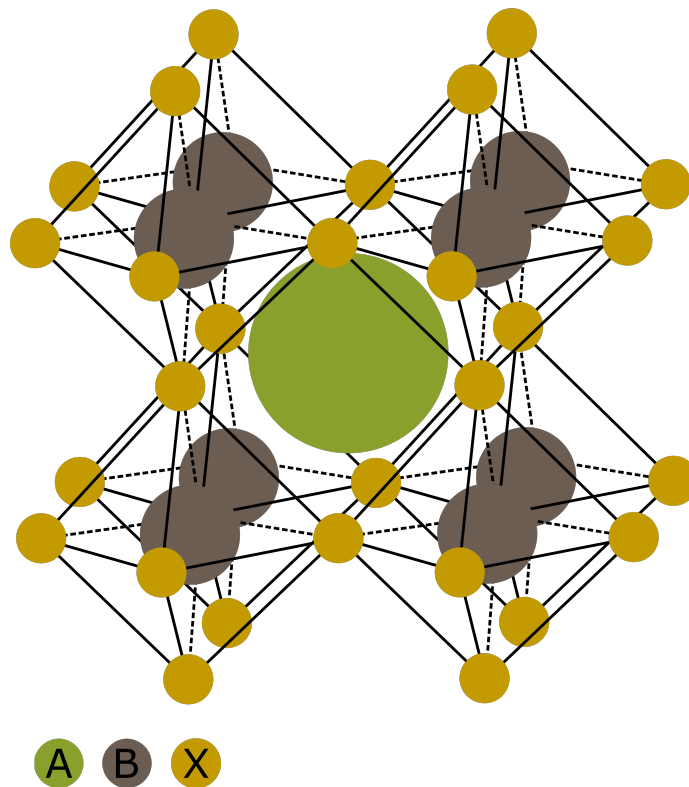
Figure 1: ABX_3 crystal structure.

Photovoltaic parameters can be influenced by a change in the morphology of the perovskite film. As already known, perovskites are highly sensitive to fabrication conditions. Therefore, the process and respective parameters critically impact the thin films morphology. Uniform and dense crystals with high reproducibility are preferred to achieve less surface area. An increase in the concentration of the stock solution leads to increased grain size. For example, for a 25 wt% $MAPbI_3$ stock solution, the average grain size is approximately 100 nm. Increasing the concentration to 45 wt%

and 55 wt% grain sizes of 300 nm and 500 nm, respectively, can be obtained. Interestingly, considering the Shockley-Read-Hall (SRH) model, the trap density decreases with increasing grain size. This results in an increase in the V_{OC}. Besides the V_{OC}, the short-circuit current (J_{SC}), the power conversion efficiency (*PCE*), and the fill factor (*FF*) also inrease [3].

1.2   Advances in hole transport materials

Hole transport materials play a crucial role in the organic-inorganic halide perovskite production. They act as a physical barrier between the anode and the perovskite layer, improve the hole transport efficiency, and influence the V_{OC}. An uniform hole transport layer leads to formation of a smooth and dense perovskite film with high surface coverage. This results in suppression of charge recombination and the increase of stability of OIHPs. One huge disadvantage of HTMs are the costs, as they are one of the more expensive materials in PSCs. Hole transport materials for OIHPs can be categorized as inorganic (graphene oxide) or organic materials. Organic HTMs (Fig. 2) can be small molecules (MeO-2PACz), polymers (PTAA), or oligomers. The selection criteria of HTMs are towards their charge extraction properties. The photovoltaic process in organic-inorganic halide perovskite solar cells takes place in two steps. First, light is absorbed in the absorption layer, and a e^-/h^+ pair is generated. The charges are separated and selectively collected on the contacts. To enable efficient hole extraction, the material should provide high hole mobility, a compatible ionization potential, and high thermal stability. High thermal stability is required due to the heat treatment steps in a typical solar cell fabrication process. To obtain compatible ionization potential, the highest occupied molecular orbital (HOMO) or valence band maximum of the HTM should match that of the perovskite [1].
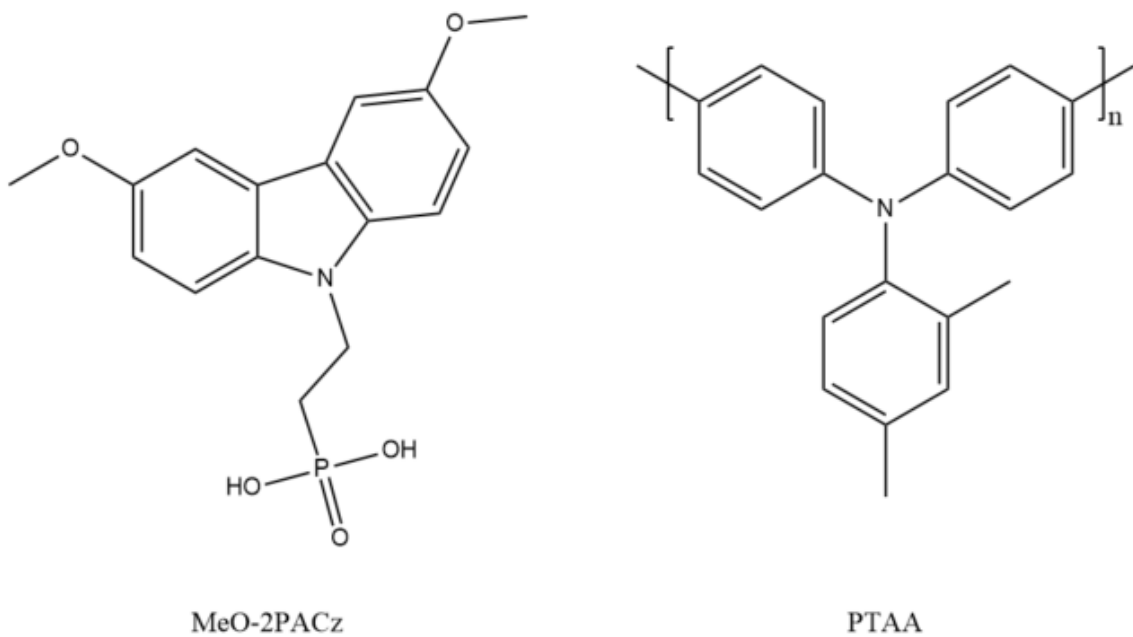
Figure 2: Used organic hole transport materials.

To reduce losses (e.g. voltage loss) between the absorber layer and the charge selective contacts, changes in the perovskite precursors can be performed. Therefore, finely-tuned processing parameters are required. Another approach is using self-assembling materials (SAM) as charge-selective contacts instead of common hole transport materials. SAMs are produced by simple dipping or spin-coating techniques, working as simple hole-selective contacts. Compared to PTAA, self-assembling materials show stronger hole-selectivities.

Carbazole derivatives, like [2-(3,6-Dimethoxy-9*H*-carbazol-9-yl)ethyl]phosphonic acid (MeO-2PACz), show electron localizing and hole-selective properties. Compared to PTAA, MeO-2PACz also shows a reduced absorption in the visible wavelength regime. Due to the ideal energetic alignment, MeO-2PACz shows higher V_{OC} when implemented in solar cells. Higher open-circuit voltages can also be the result of bulk property changes (e.g., density of trap states) and reduced non-radiative recombination [4].

1.3 Methods for band gap determination

1.3.1 Optical band gap determination

Typically, the optical band gap E_g of semiconductors with a direct band gap is determined from a Tauc plot ($(\alpha \cdot E)^2$ *vs. E*). The point of intersection of the linear fit in the onset of the absorption band gap and the baseline refers to the optical band gap [7]. However, the determination of the absorption coefficient α of OIHP films can be challenging because these materials typically suffer from high surface roughness. Consequently, light scattering at the surface of the perovskite is a dominant phenomenon. An alternative approach to determine the band gap of perovskites is to derive it from the external quantum efficiency (EQE) of perovskite solar cells. Three processes are possible for a photon traveling through a homogeneous thin film: Transmission, absorption, and reflection. The ratio of the intensity of the transmitted, absorbed, or reflected light to the incident light is called transmittance *T*, absorptance *A*, and reflectance *R*, respectively. As a consequence, the sum of these quantities is equal to unity: $T + A + R = 1$ [8]. The EQE is about the sum of absorptance and reflectance of the solar cell and, therefore, $T \approx 1 - EQE$. This relation can be used in Lambert's law (Eq. 2) to achieve Eq. 3.

$$I(z) = I_0 \cdot e^{-\alpha z} \, , \tag{2}$$

$$\alpha^2 = \frac{\ln^2(1 - EQE)}{z^2} \, , \tag{3}$$

$I(z)$ describes the intensity of the transmitted light, I_0 the intensity of the incoming light, and z the depth of the absorber layer. The band gap of a semiconductor with a direct band gap is defined in Eq. 4, where *E* refers to the photon energy [9].

$$\alpha = \frac{1}{E} \cdot \sqrt{E - E_g} \, , \tag{4}$$

When combining these two formulas, the following relation is achieved:

$$\ln^2(1 - EQE) \cdot E^2 \propto E - E_g \, , \tag{5}$$

In a plot of $\ln^2(1 - EQE) \cdot E^2$ vs. *E*, the band gap can be extracted as the intersection between the linear fit of the onset of the curve and the baseline (similar to the determination via α). The relation $(E \cdot EQE)^2 \propto E - E_g$ is achieved over the first-order series expansion of Eq. 5 close to $EQE = 0$. This method can be frequently found in the literature [5]. An example of both ways is shown in Appendix 5.5.

1.3.2   Electrochemical band gap determination

Besides their optical properties, OIHPs also show unique electronic properties. Electrochemistry is a simple and cheap tool to investigate the electronic properties of materials. Also, the detection of defects, grain boundaries and the presence of minority phases is possible via electrochemical experiments. Although electrochemistry is simple to use, it is not often used to determine the band edge position and trap state density of perovskites. The major problem is the instability of the material in almost all commonly used solvents and electrolytes. Also, the appearance of irreversible electrochemical reactions and unintended side reactions argue against this determination method. For performing electrochemical band gap determination on OIHPs it is important to know the stability window and the products formed during the redox transformation [6].

Two common electroanalytical techniques are cyclic voltammetry (CV) and electrochemical voltage spectroscopy (EVS). Important parameters for CV are the anodic and cathodic half-wave potentials, as well as their corresponding currents. Measuring the current between working electrode (WE) and counter electrode (CE) during a potential scan leads to the cyclic voltammogram. A typical voltammogram consists of a reductive and an oxidative scan. For reductive scans the potentials are applied from 0 versus reference electrode (RE) to a certain negative value and vice versa for oxidative scans.
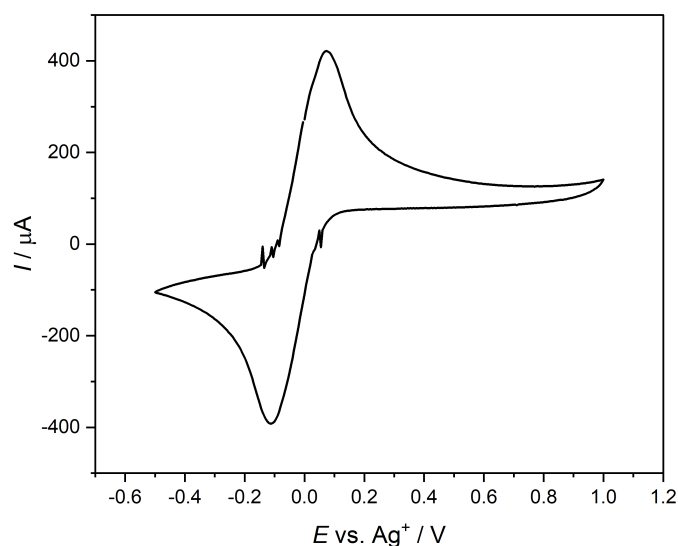

Figure 3: Typical cyclic voltammogram (calibration of the Ag/Ag$^+$ reference cell with ferrocene).

As shown in Fig. 3, the CV yields an anodic (negative current) and a cathodic (positive current) peak. The respective redox values can be described by the Nernst equation (Eq. 6) for a reversible system [10].

$$E = E^0 + \frac{0.059}{z} \cdot \log(\frac{a_{Ox}}{a_{Red}}) \ , \tag{6}$$

E stands for the electrochemical potential, E^0 for the standard electrode potential, z is the number of electrons transferred per formula unit, and a_{Ox}/a_{Red} for the activities of the oxidized and reduced species, respectively. To obtain the total redox values (half-wave potentials), the second derivative of the voltogramm is taken and set to zero (see 5.6). A straight-line is drawn through the calculated inflection point and extended to the x-axis. At the point of intersection between the drawn line and the zero current level, the total redox values can be determined.

In electrochemical voltage spectroscopy the cell current results from applying small potential steps to the cell. Thereby, the current $I(t)$ is continuously measured [11]. To obtain the absolute orbital energy, the values measured against Ag/Ag$^+$ need to be converted to vacuum level. For this, the potential is corrected by +4.75 eV vs. normal hydrogen electrode (NHE), as stated in Cardona et al. [12]. Each step is then integrated to gain the total charge ΔQ of each step (Eq. 7).

$$\Delta Q = \int_0^{t_{meas}} I(t)dt \ , \tag{7}$$

The point where ΔQ starts to deviate from the base line is taken as the reduction or oxidation potential.

E_{cal} refers to the potential of the reference electrode vs. NHE, determined from calibration with ferrocene. Eq. 8 and 9 yield the total anionic or cathodic potential. E_{VB} stands for the electrochemical potential of the valence band and E_{CB} for the electrochemical potential for the conduction band.

$$E_{VB} = -(E_{onset,ox \ vs. \ NHE} + 4.75 + E_{cal})(eV) \ , \tag{8}$$

$$E_{CB} = -(E_{onset,red \ vs. \ NHE} + 4.75 + E_{cal})(eV) \ , \tag{9}$$

2 Experimental

2.1 Materials

Table 1: Overview of used materials, including supplier, purity, and abbreviation.

Material	Supplier	Purity / %	Abbr.
Poly[bis(4-phenyl)(2,4,6-trimethylphenyl)amine]	Sigma Aldrich	-	PTAA
[2-(3,6-Dimethoxy-9H-carbazol-9-yl)-ethyl]phosphonic acid	TCI Chemicals	> 98.0	MeO-2PACz
Formamidinium iodide	-	-	FAI
Formamidinium bromide	-	-	FABr
Lead(II) iodide	Alfa Aesar	99.9985	PbI_2
Lead(II) bromide	Alfa Aesar	>98	$PbBr_2$
Cesium iodide	Alfa Aesar	99.9	CsI
Cesium bromide	Alfa Aesar	99.9	CsBr
[6,6]-Phenyl C_{61} butyric acid methyl ester	Solenne	99	$PC_{60}BM$
Bathocuproine	Ossila	>99.5	BCP
Lithium fluoride	chemPUR	99.99	LiF
Aluminium	chemPUR	99.999	Al
Silver	chemPUR	99.999	Ag
N,N-Dimethylformamide	Sigma Aldrich	99.8	DMF
Dimethyl sulfoxide	VWR chemicals	99.7	DMSO
Ethanol	VWR chemicals	>99.8	EtOH
Toluene	VWR chemicals	>99.0	-
Chloroform	Sigma Aldrich	>99.5	$CHCl_3$
Chlorobenzene	Alfa Aesar	99.8	CB
2-propanol	Merck	100	IPA
Hydrochloric Acid	VWR chemicals	37	HCl

2.2   Sample preparation

For solar cells, ITO coated glass was cut into stripes with a width of 2.5 cm and precleaned with toluene by using soft tissues. The ITO was partially masked with an adhesive tape, and acidic etching was performed by using concentrated HCl (ω(HCl)=37%). The etched substrates were cleaned with deionized H_2O, toluene, and cut into pieces (à 2.5 $\times$ 2.5 cm^2). Further cleaning was performed by using a Hellmanex solution and ultrasonic treatment (80 °C for approx. 15 min). Afterwards the substrates were washed three times with deionized water and stored in IPA.

For electrochemistry, the size of the glass substrates differs. First, ITO coated glass was cut into pieces (à 3 $\times$ 3 cm^2). The samples where prescratched on the backside with a width of 1 cm. Afterwards, the substrates where cleaned in the same way as previously mentioned. The glass substrates are divided into three pieces after perovskite application before the electrochemical measurements. This make sure that reductive and oxidative side is measured for the same film. One film is kept as backup.

All thin films are processed on the prepared ITO substrate using several spin-coating steps. Therefore, optimized spin coating recipes for each layer have to be used. The used spin coating parameters and concentrations are listed in Table 2. The general perovskite coating parameters were taken from Chen et al. [13], and modified for the used precursor solutions. One important aspect is to avoid the interaction of the different solvents. This is achieved via annealing to evaporate the volatile compounds. Also the so-called anti-solvent treatment [14] is an important technique to improve the surface coverage and the film smoothness of the $FA_{0.8}Cs_{0.2}Pb(I_{1-X}Br_X)_3$ perovskite thin films. The anti-solvent, here chlorobenzene, is applied dropwise during spinning within approximately 1 s.

Spin coating is performed under inert conditions (nitrogen atmosphere) at room temperature.
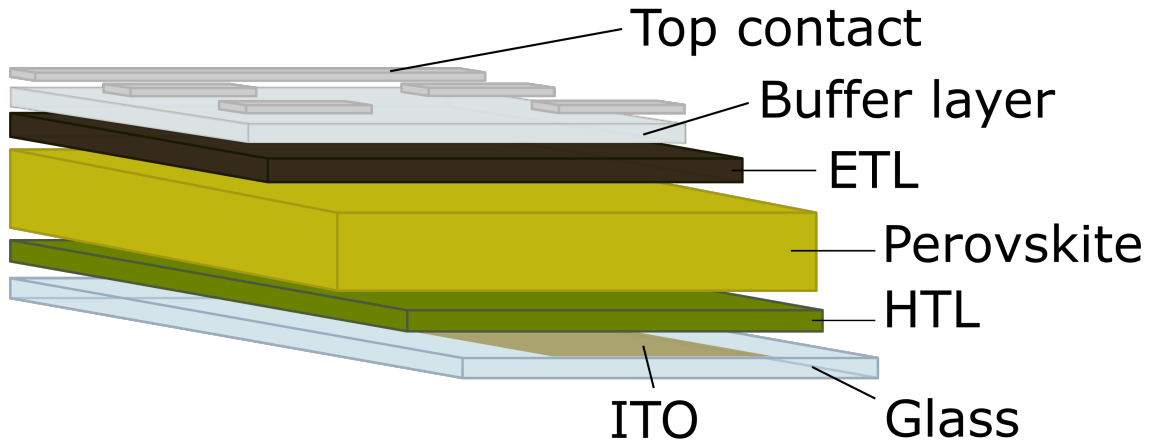
Figure 4: Schematic figure of a p-i-n lead halide perovskite solar cell.

Table 2: Used spin coating parameters for different thin films.

| Material | c mg/mL | spin coating | | | annealing | |
		speed rpm	ramp rpm s-1	time s	time min	heat °C
PTAA	1.5	100	3	25	-	-
		100	1	1	10	100
DMF	-	67	2	2	-	-
		67	1	1	-	-
MeO-2PACz	0.3	50	2	26	-	-
		50	1	1	10	100
Perovskite	-	8	1	1	2	65
		67	2	58	10	100
$PC_{60}BM$	20	22	2	16	-	-
		33	2	15	-	-
BCP	0.2	83	2	26	-	-
		83	1	1	-	-

2.2.1 Processing of PTAA thin films as hole transport layers

PTAA solutions (120 μL, 1.5 mg L^{-1}, dissolved in toluene) is spin-coated on pre-etched ITO substrates (à 2.5 × 2.5 cm^2). After coating, heat treatment is performed on a heating plate at 100 °C for 5 min. Subsequently, the samples are patterned with a cotton swab on the edges using toluene (30 μL) and annealed at 100 °C for a further 5 min. Annealing ensures that the applied thin film is more stable to the solvents of the further coated top layers. Patterning has to be performed to provide a contact in the solar cell device between the ITO and the top-electrode.

2.2.2   Processing of MeO-2PACz thin films as hole transport layers

The MeO-2PACz solution (120 µL, 0.2 mg mL^{-1}, dissolved in absolute Ethanol) is processed on ITO coated glass substrates (à 2.5 × 2.5 cm^2 for solar cells, à 3 × 3 cm^2 for electrochemistry). The coated film is heat-treated at 100 °C for 5 min, patterned with absolute EtOH, and further annealed at 100 °C for 5 min.

2.2.3   Processing of FA$_{0.8}$Cs$_{0.2}$Pb(I$_{1-x}$Br$_X$)$_3$ thin films

First, the hole transport layers have to be pretreated before applying the perovskite layer. In case of PTAA, DMF is used as a wetting agent. 140 µL DMF is applied via spin coating to the hole transport layer surface.
Using MeO-2PACz as a transport layer, the pretreatment is slightly different. Instead of using the previously mentioned wetting technique, absolute EtOH (150 µL) is dispersed during spinning, using the same coating parameters as for the perovskite. Only the spinning time was adjusted to 20 s instead of 59 s. The whole wetting agent is applied within 1 s. Immediately after, the perovskite thin films are processed (180 µL) on top of the hole transport layer. After 24 s the thin film is treated with chlorobenzene as antisolvent. Annealing is then performed at 65 °C for 2 min and at 100 °C for 10 min. The bromide concentrations varies from ω(Br) = 0% up to ω(Br) = 100% in steps of 20% (described as X in the general formula FA$_{0.8}$Cs$_{0.2}$Pb(I$_{1-x}$Br$_X$)$_3$). All used precursors and weights for 1 mL solution are listed in Table 3. Perovskites with a bromide content from ω(Br) = 0% to ω(Br) = 60% are dissolved in DMF/DMSO (solvent ratio of 85:15) and yield a concentration of 1.08 mol L^{-1}. To dissolve ω(Br) = 80% and ω(Br) = 100% perovskites properly, the solvent ratio is shifted to 70:30 and a concentration of 0.90 mol L^{-1}. The dissolved precursor solutions are heated at 65 °C for 1 h, before spin coating.

Table 3: Used precursors and weigths for a 1 mL perovskite solution, dissolved in DMF/DMSO.

Perovskite	precursor / mg					
	FAI	FABr	PbI$_2$	PbBr$_2$	CsI	CsBr
FA$_{0.8}$Cs$_{0.2}$PbI$_3$	148.6	-	497.9	-	56.2	-
FA$_{0.8}$Cs$_{0.2}$Pb(I$_{0.8}$Br$_{0.2}$	148.6	-	348.5	118.9	56.2	-
FA$_{0.8}$Cs$_{0.2}$Pb(I$_{0.6}$Br$_{0.4}$)$_3$	148.6	-	199.1	237.9	56.2	-
FA$_{0.8}$Cs$_{0.2}$Pb(I$_{0.4}$Br$_{0.6}$)$_3$	148.6	-	47.5	356.8	56.2	-
FA$_{0.8}$Cs$_{0.2}$Pb(I$_{0.2}$Br$_{0.8}$)$_3$	74.3	36.0	-	330.3	28.1	15.3
FA$_{0.8}$Cs$_{0.2}$PbBr$_3$	-	90.0	-	330.3	-	38.4

2.2.4 Processing of PC$_{60}$BM thin films as electron transport layers

On top of the respective perovskite, PC$_{60}$BM is processed as an electron transport layer (ETL). 150 µL of the PC$_{60}$BM solution (20 mg mL^{-1}, dissolved in CF/chlorobenzene, solvent ration 3:1) is applied to the perovskite surface and spin-coated.

2.2.5 Processing of the BCP thin film (as buffer layer)

The BCP thin film (0.2 mg mL^{-1}, dissolved in IPA) is used as an bufferlayer to increase the charge carriers extraction efficiency between the top contact and the ETL. To investigate the influence of the film thickness, different concentrations of the BCP solution (from 0.1 mg mL^{-1} to 0.5 mg mL^{-1}) are processed in the same way.

2.2.6 Processing of the silver top contact layer

The silver contact is applied by evaporating solid silver on top of the solar cells using an Edwards Auto 500 as evaporation system. An evaporation mask is used as a sample holder to obtain a specific shape of the electrodes. Via controlling the current, a thickness of 100 nm is evaporated.

2.2.7 Processing of the LiF/Al top contact layer

In some cases lithium fluoride and aluminum are processed as alternative top layers on the PC$_{60}$BM thin-films. First, lithium fluoride (0.5 nm) is evaporated on the PC$_{60}$BM. Afterwards, a 100 nm aluminum thin film is evaporated on top.

2.3 IV-characterization

The IV characterization was performed under AM1.5G illumination (LOT-Quantum Design: Xenon arc lamp with filter). The voltage is changed from -1 to 1.5 V and the current is detected by using a source measure unit (Keithley 2401 Source Meter). The intensity of the simulated sun spectra is determined with a calibrated silicon solar cell (Mencke&Tegtmeyer).

2.4 EQE

For the external quantum efficiency detection, the current is measured using a potentiostat (Jaissle 1002 T-NC) and a lock amplifier (Stanford Research system SR830 DSP). A xenon arc lamp (LOT-Quantum Desing) is used as light source. A holographic grating monochromator (Corner Stone 130 1/8 m) is used to gain

monochromatic light. To obtain comparable results, calibration with a silicon photodiode (Hamamatsu S2281) is carried out.

The EQE was calculated via the detected current obtained fopr each excitation wavelength. For measurements close to the band gap, a second measurement was performed for each solar cell to determine the exact band gap value. For this the lamp was adjusted to the respective band gap region. Also, additional long pass filters (see Table 4) were used to eliminate background noises. Finally, the exact measurements in the band gap region were combined with the whole spectra measurements and depicted in Fig. 8.

Table 4: Overview measurements in the band gap region for LiF/Al and BCP/Ag.

Perovskite	amplification	longpass filters / nm
$FA_{0.8}Cs_{0.2}PbI_3$	1000	830
$FA_{0.8}Cs_{0.2}Pb(I_{0.8}Br_{0.2})_3$	1000	760
$FA_{0.8}Cs_{0.2}Pb(I_{0.6}Br_{0.4})_3$	1000	700, 715
$FA_{0.8}Cs_{0.2}Pb(I_{0.4}Br_{0.6})_3$	1000	745
$FA_{0.8}Cs_{0.2}Pb(I_{0.2}Br_{0.8})_3$	1000	630
$FA_{0.8}Cs_{0.2}PbBr_3$	1000	540, 550

2.5 Electrochemistry

All electrochemical measurements were carried out under inert conditions. For recording, a Jaissly Potentiostat-Galvanostat (IMP 88 PC-10) was used. Cyclic voltammetry and electrochemical voltage spectroscopy are the chosen electroanalytical determination methods.

The setup consists of a working electrode, a reference electrode, and a counter electrode, as shown in Fig. 5. As a RE, a Ag/Ag$^+$ (AgNO$_3$ in dichloromethane) electrode and as a CE, a platinum plate is used. Lead halide perovskite thin films coated on MeO-2PACz and ITO/glass substrates (à 1 $\times$ 3 cm^2) were used as WE [6]. A self-made RE was used in this setup, because common quasi-RE require calibration with ferrocene after every experiment. Ferrocene reacts with the dissolved products of perovskite decomposition and a precipitate, which interferes the measurement, is formed.
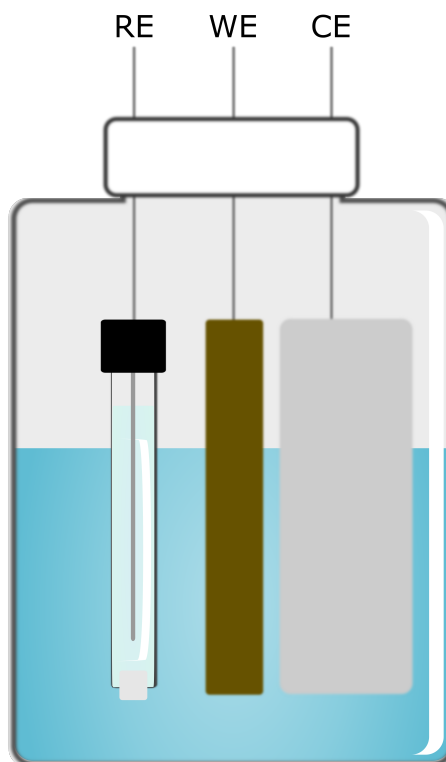
Figure 5: Schematic measurement setup of the electrochemical band gap determination, including a working electrode (WE), a reference electrode (RE), and a counter electrode (CE).

2.6 Photoluminescence

Photoluminescence (PL) is measured by exciting the perovskite thin films on Me-2PACz and ITO/glass with a laser (Coherent Obis, excitation wavelength = 488 nm, power = 5 mW). Different long-pass filters are used for shielding the excitation light (550 nm, 610 nm). A CCD sensor attached to a Shamrock 303i monochromator equipped with 150 lines/mm, blaze 800 nm grating is used to acquire the emitted photoluminescence (Andor DV420A-OE).

2.7 Surface topography

To determine the surface roughness of lead halide perovskite thin films, a Brucker DekTak XT stylus profilemeter is used.
For the scanning electron microscopy (SEM) measurements, a JEOL JSM-6360 LV microscope with a Bruker Nano X-Flash detector is used.

3 Results and discussion

The goal of this thesis was to investigate the band gap of different lead halide perovskites of the type $FA_{0.8}Cs_{0.2}Pb(I_{1-X}Br_X)_3$. Different perovskite compositions have a direct impact on the crystal structure: Increasing the bromide content increases the band gap of the perovskite thin films. All processed devices are characterized by IV character-ization. To determine the band gap, two different approaches are used. On the one side, optical determination via the EQE curves is used. On the other side, the band gap is determined electrochemically.

3.1 Photovoltaic performance

Spin coating and evaporation deposition were chosen to produce solar cells. Comparing PTAA and MeO-2PACz layers (see 5.2) in an optimized perovskite recipe [13] an increase of at least 5 % FF for MeO-2PACz was measured. However, this specific compositions open-circuit voltage and short-circuit current remain nearly identical. The power conversion efficiency slightly increased from 10.1% up to 10.7%. Although the compared hole transport layers yield similar results, MeO-2PACz was the material of choice for further experiments. As stated in the literature [15], MeO-2PACz can be used to suppress phase segregation. Lin et al. [16] stated also, that the used material induces significant changes in ITO electrodes work function upon chemical functionalization. Compared to other hole transport layers, this significant improvements were key arguments utilizing this material.

LiF and BCP are widely used as interfacial layers between the ETL and the top electrode. In this thesis, both were used and compared for different variations in the perovskites halide ratio. LiF/Al systems are well-established contact layers in organic solar cells. They yield constant results and are reproducible. BCP/Ag is also a well-established contact layer in perovskite solar cells. For BCP several concentrations were tested to obtain the best working parameters (see 5.1). Overall, the 0.2 mg mL^{-1} solution shows the best performance and is chosen as the best concentration. Also, as stated in Chen et al. [13], the BCP buffer's thickness significantly affects the J_{SC} and the *FF*. A lower concentrated solution results in smaller serial resistances. Silver electrodes tempt to undergo degradation processes over time. Due to chemical degradation a metal-organic interlayer is formed, improving the device's performance for a certain time [17].

To determine the best working conditions with the introduced hole transport layer, the recipie had to be adjusted. This goal was achieved via variations in the halide content of the $FA_{0.8}Cs_{0.2}Pb(I_{1-X}Br_X)_3$ perovskite. The color change (see Fig. 6) caused by the increasing bromide content was the most striking and visible transition.
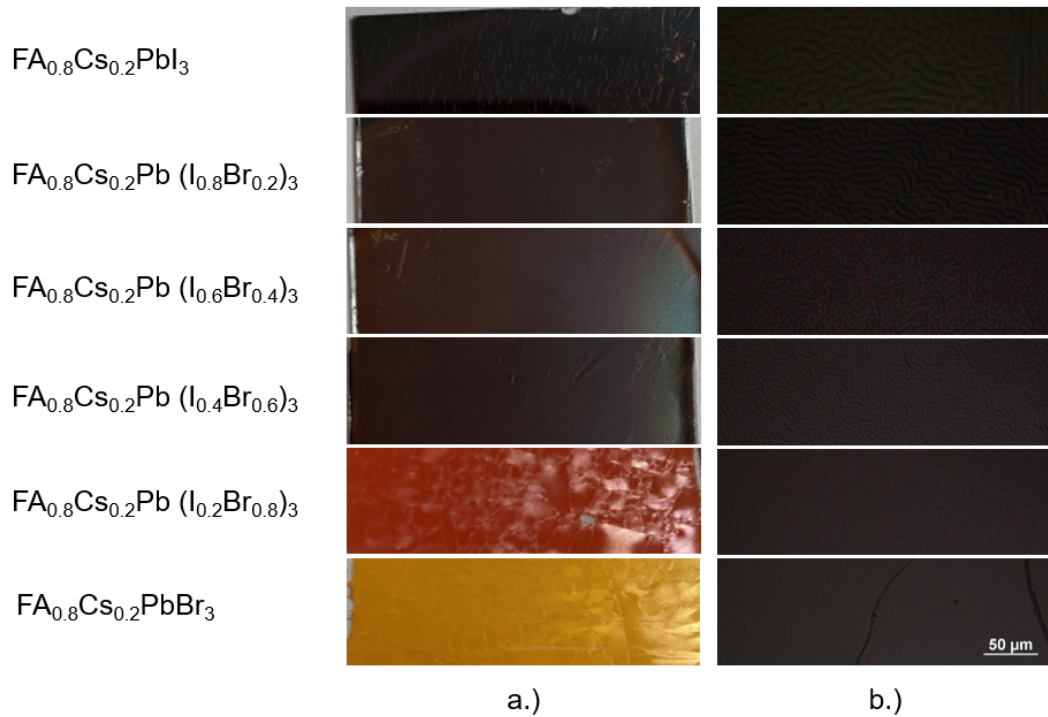

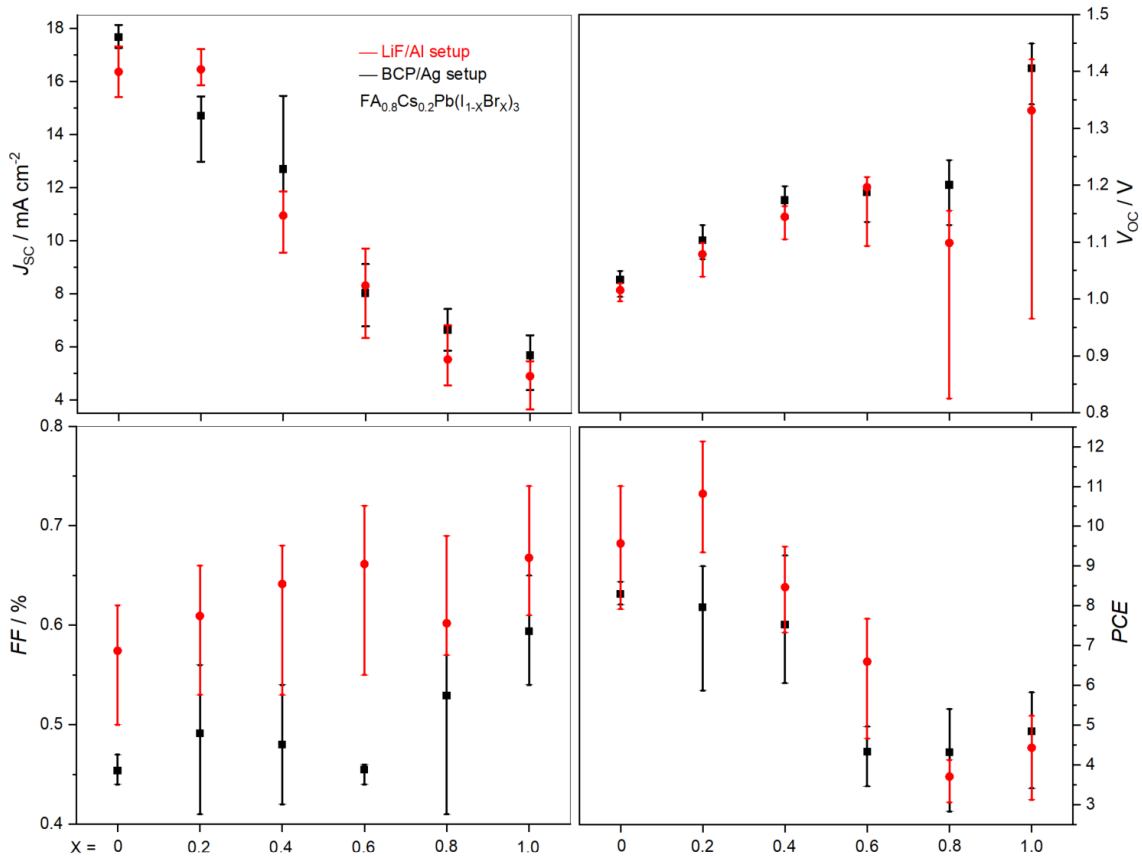**Figure 6:** Recorded surface pictures of lead halide perovskite thin films from camera (a.)) and SEM (b.)).

Figure 7: Comparing J_{SC}, V_{OC}, FF, and PCE of two perovskite solar cell systems with different halide contents. BCP/Ag (black) and a LiF/Al (red) are used as top-contact layers.

Fig. 7 shows the J_{SC}, V_{OC}, FF, and PCE values of the different lead halide perovskite compositions. As visible in Fig. 7 and Table 6, the range as well as the mean values of the measured data are given (further data see 5.3).

Fig. 7 shows direct correlations in J_{SC} and V_{OC} between the halide content and the obtained results. The measured short circuit current decreased with increasing bromide content. Therefore, the highest J_{SC} is obtained in a pure iodine perovskite solar cell and yields $18.13 \, \text{mA cm}^{-2}$. The open-circuit voltage behaves exactly the opposite and increases up to 1.4 V. Overall, solar cells with LiF/Al perform significantly better than the BCP/Ag solar cells. The theoretical $V_{OC, loss}$ can be determined, by calculating the theoretical V_{OC} via $V_{OC,th} \leq \frac{E_{g, opt.}}{q}$ (see Table 5). The optical measured band gap values are taken for $E_{g, opt.}$.

Table 5: Calculated theoretical loss in V_{OC}.

Perovskite	$V_{OC, meas}$ / V	$V_{OC, th}$ / V	$V_{OC, loss}$ / V	$V_{OC, loss}$ / %
$FA_{0.8}Cs_{0.2}PbI_3$	1.04	1.56	0.52	33
$FA_{0.8}Cs_{0.2}Pb(I_{0.8}Br_{0.2})_3$	1.12	1.67	0.55	33
$FA_{0.8}Cs_{0.2}Pb(I_{0.6}Br_{0.4})_3$	1.18	1.79	0.61	34
$FA_{0.8}Cs_{0.2}Pb(I_{0.4}Br_{0.6})_3$	1.21	1.71	0.50	29
$FA_{0.8}Cs_{0.2}Pb(I_{0.2}Br_{0.8})_3$	1.20	2.07	0.87	42
$FA_{0.8}Cs_{0.2}PbBr_3$	1.44	2.27	0.83	37

$FA_{0.8}Cs_{0.2}Pb(I_{0.2}Br_{0.8})_3$, and $FA_{0.8}Cs_{0.2}PbBr_3$ shows a higher loss in V_{OC}. The used measured V_{OC} values ($V_{OC, meas}$) where averaged values from both top contacts listed in Table 6. The measured optical band gap for $FA_{0.8}Cs_{0.2}Pb(I_{0.4}Br_{0.6})_3$ is lower than expected and therefore it yields the smallest $V_{OC, loss}$ value. However, the $V_{OC, loss}$ increases with increasing bromide content. Also, as expected, larger band gaps are measured with increasing bromide content. Beside the high voltage output at higher bromide content, higher fill factors are measured. As stated in Ryu et al. [18], the fill factor increases due to the broader band gap and the superior hole mobility of the perovskite. The diagram shows that the LiF/Al contacts lead to higher fill factors (max. values) than the BCP/Ag. The highest fill factor is obtained in $FA_{0.8}Cs_{0.2}PbBr_3$ perovskite solar cells (74 %) using LiF/Al as top contacts.

As visible in Fig. 7, the power conversion efficiency shows no clear trend. It can be stated that the pure bromide perovskite yield the lowest PCE. A maximum of 12% is measured in $FA_{0.8}Cs_{0.2}Pb(I_{0.8}Br_{0.2})_3$ solar cells with LiF/Al. As stated in Ameen et al. [19], the power conversion efficiency strongly depends on the interaction between the perovskite and HTM during fabrication.

Table 6: Measured J_{SC}, V_{OC}, *FF*, and *PCE* of two perovskite solar cells with different halide contents

Perovskite	top contacts	J_{SC} / mA cm^{-2}			V_{OC} / V		
		min	max	mean	min	max	mean
$FA_{0.8}Cs_{0.2}PbI_3$	BCP/Ag	17.3	18.1	17.7	1.00	1.05	1.03
	LiF/Al	15.4	17.3	16.4	1.00	1.03	1.02
$FA_{0.8}Cs_{0.2}Pb(I_{0.8}Br_{0.2})_3$	BCP/Ag	13.0	15.4	14.7	1.07	1.13	1.10
	LiF/Al	15.9	17.2	16.5	1.04	1.10	1.08
$FA_{0.8}Cs_{0.2}Pb(I_{0.6}Br_{0.4})_3$	BCP/Ag	10.9	15.5	12.7	1.14	1.20	1.17
	LiF/Al	7.3	10.9	9.5	1.11	1.16	1.14
$FA_{0.8}Cs_{0.2}Pb(I_{0.4}Br_{0.6})_3$	BCP/Ag	6.8	9.7	8.0	1.19	1.20	1.19
	LiF/Al	6.3	9.7	8.3	1.09	1.21	1.20
$FA_{0.8}Cs_{0.2}Pb(I_{0.2}Br_{0.8})_3$	BCP/Ag	5.9	7.4	6.6	1.13	1.24	1.20
	LiF/Al	4.6	6.8	5.5	0.83	1.16	1.10
$FA_{0.8}Cs_{0.2}PbBr_3$	BCP/Ag	4.4	6.4	5.7	1.34	1.45	1.41
	LiF/Al	3.6	5.5	4.9	0.97	1.42	1.33

Perovskite	top contacts	*FF* / %			*PCE* / %		
		min	max	mean	min	max	mean
$FA_{0.8}Cs_{0.2}PbI_3$	BCP/Ag	44	47	45	8.0	8.6	8.3
	LiF/Al	50	62	57	7.9	11.0	9.6
$FA_{0.8}Cs_{0.2}Pb(I_{0.8}Br_{0.2})_3$	BCP/Ag	42	56	49	5.9	9.0	8.0
	LiF/Al	53	66	61	9.4	12.1	10.8
$FA_{0.8}Cs_{0.2}Pb(I_{0.6}Br_{0.4})_3$	BCP/Ag	42	54	48	6.1	9.3	7.5
	LiF/Al	53	68	64	7.3	9.5	8.5
$FA_{0.8}Cs_{0.2}Pb(I_{0.4}Br_{0.6})_3$	BCP/Ag	44	46	46	4.3	9.1	6.8
	LiF/Al	55	72	66	4.7	7.7	6.6
$FA_{0.8}Cs_{0.2}Pb(I_{0.2}Br_{0.8})_3$	BCP/Ag	41	60	53	2.8	5.4	4.3
	LiF/Al	57	69	60	3.1	4.1	3.7
$FA_{0.8}Cs_{0.2}PbBr_3$	BCP/Ag	54	65	59	3.4	5.8	4.9
	LiF/Al	61	74	67	3.1	5.2	4.4

3.2   Optical and electrochemical band gap determination

One primary goal of this thesis was to investigate the comparability of optical and electrochemical band gap determination methods. The optical band gap was determined via the external quantum efficiency. For that the previously described solar cells were used as samples. Cyclic voltammetry and electrochemical voltage spectroscopy were the method of choice to determine the band gaps electrochemically. However, to determine the electrochemical band gap, or more precisely, the VB-CB levels of perovskites, perovskite thin films on MeO-2PACz and ITO/glass substrates were used.
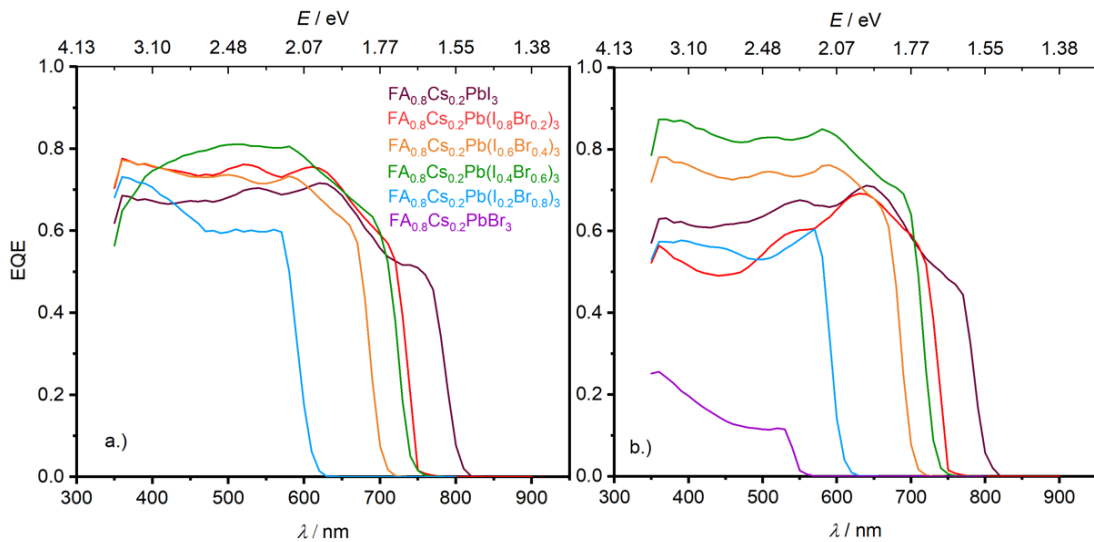
3.2.1 Optical band gap determination

Figure 8: EQE curves of LiF/Al (a.)) and BCP/Ag (b.)) solar cells.

Fig. 8 shows the calculated EQE values for lead halide solar cells. Both graphs show some unexpected behavior regarding the $FA_{0.8}Cs_{0.2}Pb(I_{0.4}Br_{0.6})_3$ samples. As considered previously, the band gap should increase with increasing bromide content. As it is visible, this is not the case for this composition. One possible reason could be that the perovskite preparation process for this composition did not work well and must be adjusted. The internal resistance of the LiF/Al sample with 100% Br was probably too high and therefore it was not possible to determine the EQE with the equipment available. Also, in the case of the BCP/Ag solar cell, this might be an explanation why the yielded external quantum efficiency is low.
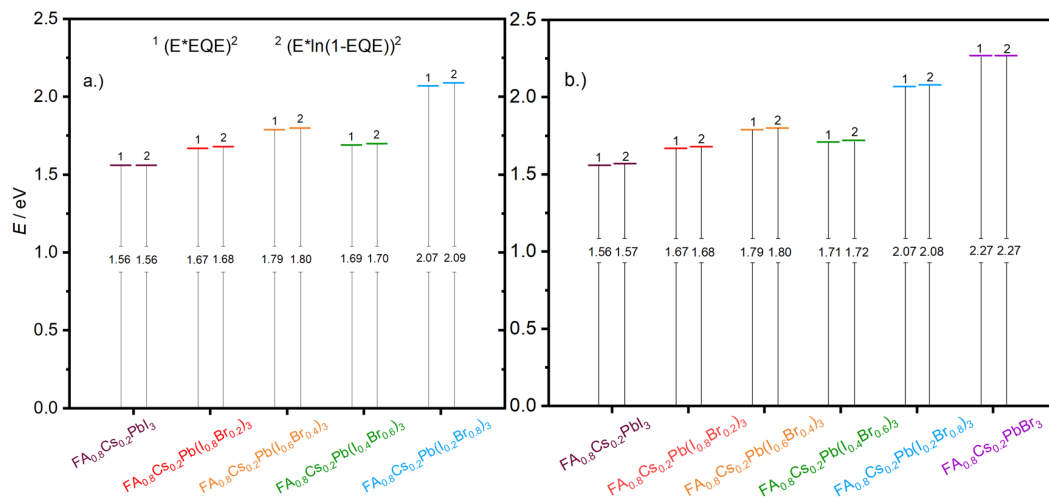
Figure 9: Calculated band gaps of LiF/Al (a.)) and BCP/Ag (b.)) solar cells in eV.

3.2.2   Electrochemical VB-CB determination

As stated previously, the VB-CB levels of perovskites were determined with two different electrochemical approaches. Only one cycle was performed per anodic/cathodic run, because the perovskite decomposes under the strong anodic/cathodic condition. The MeO-2PACz layer is required to enable optimum conditions for the perovskite to be formed. To exclude an influence of MeO-2PACz on the electrochemical measurement, a blank measurement was performed (only MeO-2PACz on ITO/glass). It turned out that the very thin hole transport layer does not affect the measurement (see 5.4).
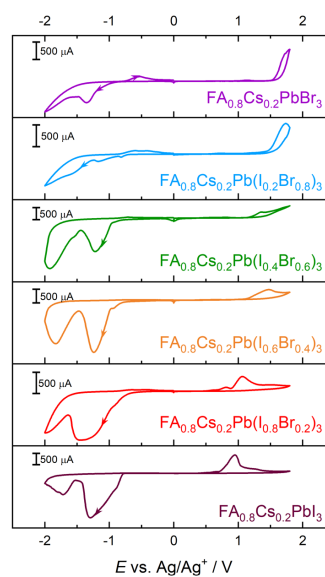
Figure 10: Measured CV curves of the perovskite thin films.

Fig. 10 shows the electrochemically detected CV-curves of the different lead halide perovskite thin films. The oxidation potential, which represents the level of the VB, increases with increasing bromide content. Conversely, the reduction potential (for calculating the CB level) remains roughly at the same level. In addition to the CV curves, EVS measurements were performed from each perovskite composition.
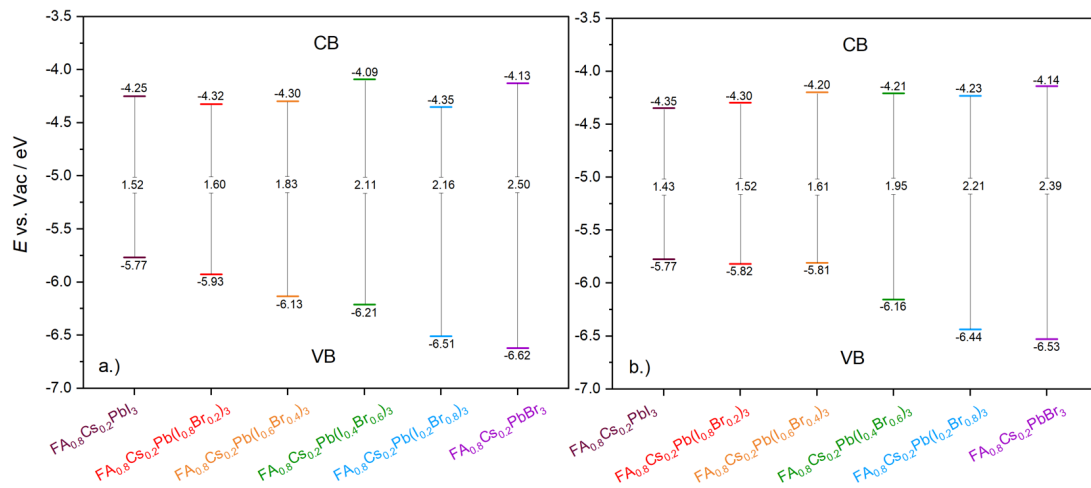
Figure 11: Calculated VB-CB levels from the CV/EVS-curves. In figure a.) the CV values and in figure b.) the EVS values are depicted.

As Fig. 11 shows, both determination methods yield comparable results. The determined EVS values are slightly smaller than the CV values. This is can be due to the chosen measurement intervals at the EVS measurement.

3.2.3   Comparison of the optical and electrochemical band gap

Table 7: Measured optical and electrochemical band gaps.

	band gap / eV			
Method	$(E*EQE)^2$	$(E*ln(1-EQE))^2$	**CV**	**EVS**
$FA_{0.8}Cs_{0.2}PbI_3$	1.56	1.56	1.52	1.43
$FA_{0.8}Cs_{0.2}Pb(I_{0.8}Br_{0.2})_3$	1.67	1.68	1.60	1.52
$FA_{0.8}Cs_{0.2}Pb(I_{0.6}Br_{0.4})_3$	1.79	1.80	1.83	1.61
$FA_{0.8}Cs_{0.2}Pb(I_{0.4}Br_{0.6})_3$	1.70	1.71	2.11	1.95
$FA_{0.8}Cs_{0.2}Pb(I_{0.2}Br_{0.8})_3$	2.07	2.08	2.16	2.21
$FA_{0.8}Cs_{0.2}PbBr_3$	2.27	2.27	2.50	2.39

Table 7 contains the band gap values determined from the two optical determination methods and from the CV and EVS derived data for every perovskite composition. Looking at the low bromide region, all four methods yield similar values. Above a bromide content of 60%, the data begin to differ. The electrochemically determined band gaps broaden with increasing bromide content and therefore, follow the trend. The optically determined bandgaps at 60 % bromide are lower than those at 40%. The electrochemical determined one is significantly higher than the others. A possible reason could be that charge carrier injection barriers between electrode and electrolyte are present, which results in higher values. As stated in literature [3], optically determined band gaps strongly depend on the homogenity of the material. The optical band gap is lower if scattering appears (due to the presence of opaque layers) in the high bromide perovskite solar cells.

3.3   Photoluminescence measurements

Photoluminescence measurements were performed to gain more information on the optical properties of the lead halide perovskite solar cells.
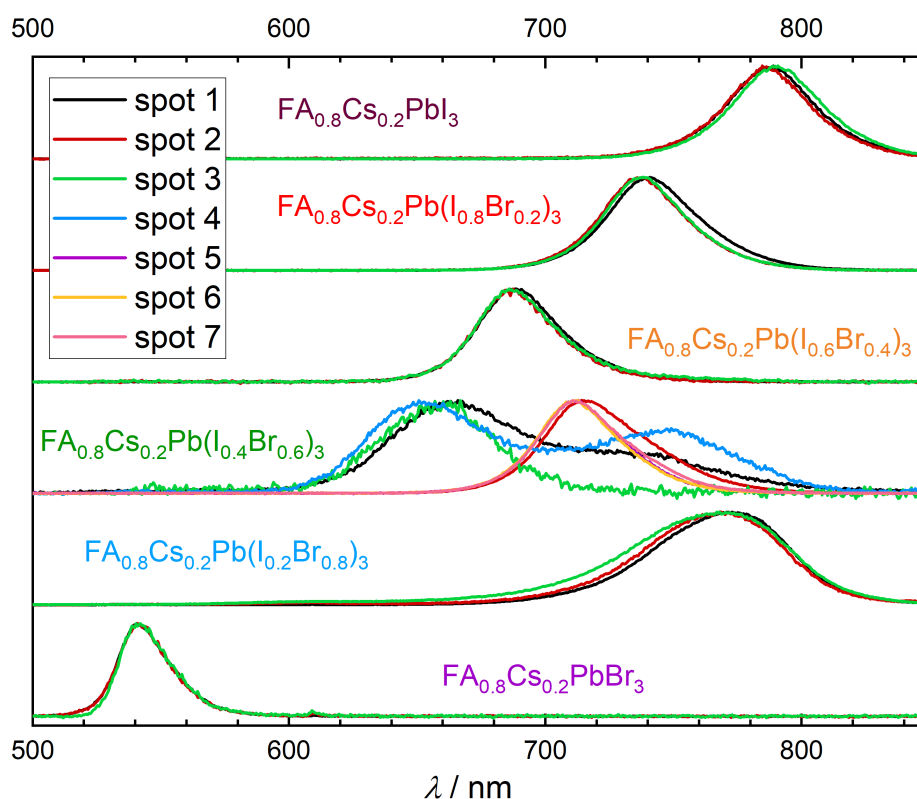
Figure 12: Recorded photoluminescence spectra of lead halide perovskite thin films.

The signal of the 80% bromide sample is shifted. It is not clear why the determined wavelength differs strongly from the one measured in the EQE setup. Looking at the 60% bromide sample, different signals at several wavelengths appear. As stated by Hoke et al. [15], this findings may refer to photo-induced phase segregation.

3.4 Surface roughness

To get a deeper insight into the optical anomalies detected previously, surface structure analyses were performed.
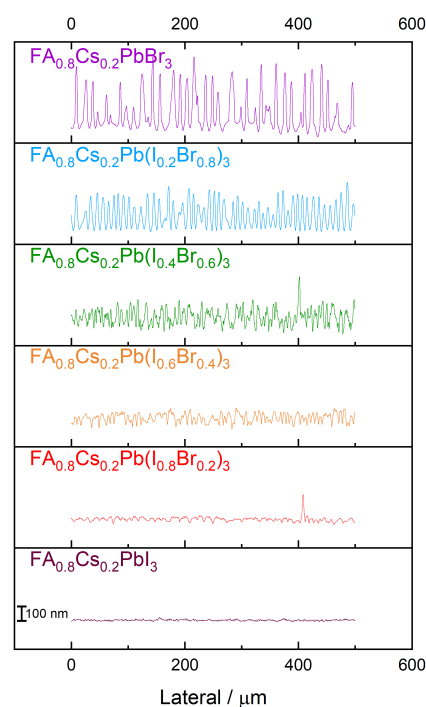
Figure 13: Normalized surface roughness of lead halide perovskite thin films.

As Fig. 13 shows, the surface roughness increases with the bromide content. The pure iodine perovskite thin film has a surface roughness of 35 nm, whereas pure bromide devices ranges 400 to 500 nm.

4   Conclusion and outlook

For certain applications, band gap tuning is an useful tool. Especially for tandem solar cells or LEDs, precise band gaps are of high interest. Too large or too low band gaps yield inefficiency in working performance. To determine the absolute band gap of solar cells, no interaction between the different layer interfaces should occur. Therefore, optimizing the perovskite composition and band gap determination techniques are necessary to get the best photovoltaic properties of PSCs. In this thesis, lead halide perovskites with the general formula $FA_{0.8}Cs_{0.2}Pb(I_{1-X}Br_X)_3$ were tested in solar cells in p-i-n configuration. Changing the perovskite composition affects the morphology of the perovskite significantly and therefore the band gap. Investigating these modifications by their optical and electrical properties was one major part of this thesis. Two different buffer layer/top contact layer combinations were investigated to compare both and check the performance of the perovskite thin layers in different systems. Comparing the fill factors of all perovskite compositions, $FA_{0.8}Cs_{0.2}Pb(I_{0.4}Br_{0.6})_3$ in a system with LiF/Al yields comparable results as pure bromide perovskites. Furthermore, yielding a maximum V_{OC} of 1.21 V and a maximum J_{SC} of 9.7 mA cm^{-2} (further data see Appendix 5.3), this solar cell composition can be interesting for tandem solar cell devices. Overall, six different perovskite compositions were tested. Beginning with a pure iodine perovskite ($FA_{0.8}Cs_{0.2}PbI_3$) the bromide content was increased in steps of 20% up to a bromide content of 100% ($FA_{0.8}Cs_{0.2}PbBr_3$). Optoelectronic and electro-chemical analysis showed that the bandgap increases with increasing bromide content. Changing the band gap of PSCs, by varying the halide content, influences all photovoltaic parameters. Referring to the IV characteristics, the fill factor and open-circuit voltage increase with increasing bromide content, contrary to the short-circuit voltage decrease.

Optical bandgap determination via external quantum efficiency detection is a commonly used method. Due to the fact that EQE curves are mostly influenced by the reflectance and transmittance of the material, any opaque layer has a huge influence on the result. Electrochemical band gap determination, on the other hand, has to deal with the resistance between the semiconductor/electrolyte interface. Overall, comparing LiF/Al and BCP/Ag, they yield similar band gaps for nearly all perovskite compositions. This indicates the validity of electroanalytical analysis for perovskites. Electrochemical measurements of perovskite solar cells are a quick and informative method. Further investigation on the stability of perovskites in different solvents and improvement of the measurement setup could lead to new possibilities.

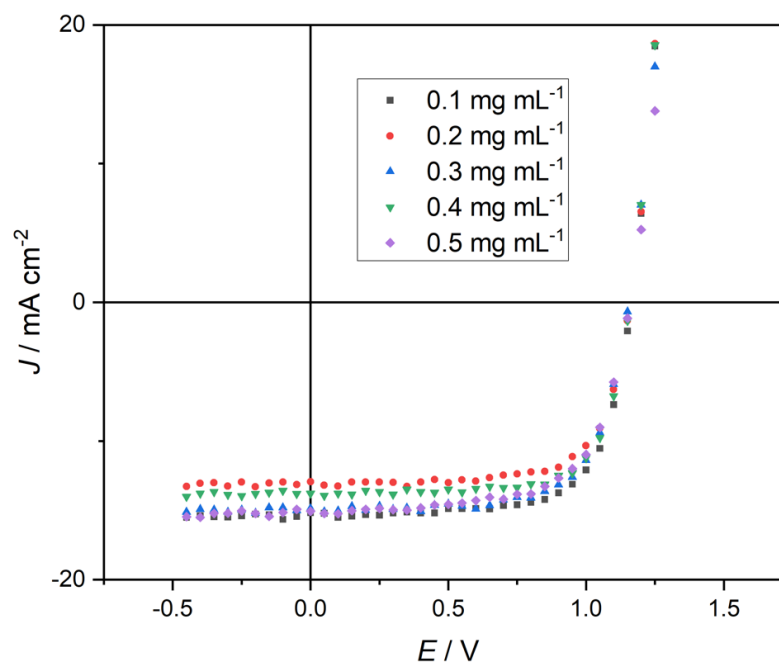# 5 Appendix

5.1 Optimization of BCP concentration

Figure 14: Measured solar cells with different BCP concentrations

Table 8: Measured performances (max. values) of solar cells with different BCP concentrations

Concentration / mg mL-1	J_{SC} / mA cm^{-2}	V_{OC} / V	FF / %	PCE / %
0.1	15.2	1.15	71	12.7
0.2	15.9	1.16	73	12.8
0.3	14.9	1.15	69	11.8
0.4	13.8	1.15	73	11.6
0.5	15.1	1.15	65	11.3

5.2   Comparing of MeO-2PACz vs. PTAA
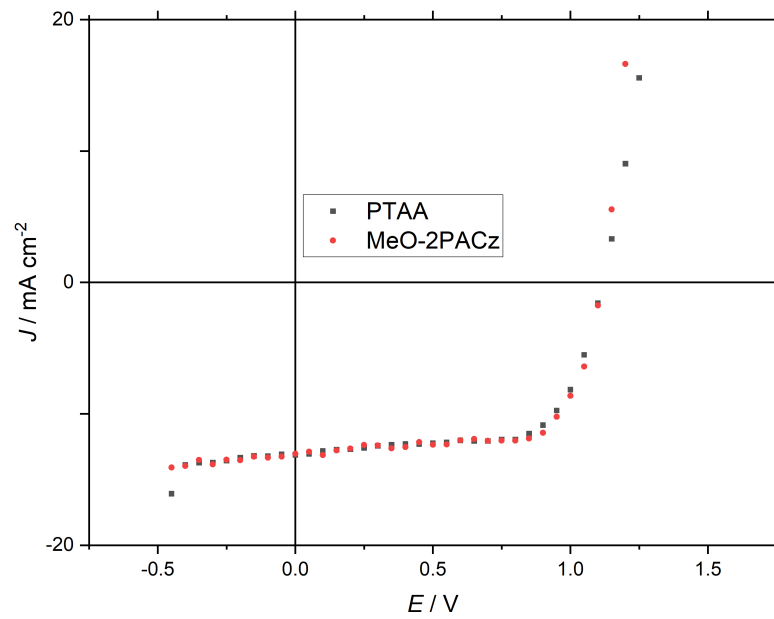
Figure 15: IV characterization curves of PTAA and MeO-2PACz.

Table 9: IV characterization (max. values) of MeO-2PACz and PTAA

HTM	J_{SC} / mA cm^{-2}	V_{OC} / V	FF / %	PCE / %
MeO-2PACz	13.0	1.11	70	10.7
PTAA	13.1	1.10	65	10.2

5.3 IV curves of solar cells with varied halide content

Table 10: Averaged IV characterization datas.

BCP/Ag	J_{SC} / mA cm^{-2}	V_{OC} / V	FF / %	PCE / %	n
$FA_{0.8}Cs_{0.2}PbI_3$	17.7 (18.1)	1.03 (1.05)	45 (47)	8.3 (8.6)	5
$FA_{0.8}Cs_{0.2}Pb(I_{0.8}Br_{0.2})_3$	14.7 (15.4)	1.10 (1.13)	49 (56)	8.0 (9.0)	10
$FA_{0.8}Cs_{0.2}Pb(I_{0.6}Br_{0.4})_3$	12.7 (15.5)	1.17 (1.20)	48 (54)	7.5 (9.3)	17
$FA_{0.8}Cs_{0.2}Pb(I_{0.4}Br_{0.6})_3$	8.0 (9.1)	1.19 (1.20)	46 (46)	4.3 (9.1)	10
$FA_{0.8}Cs_{0.2}Pb(I_{0.2}Br_{0.8})_3$	6.6 (7.4)	1.20 (1.24)	53 (60)	4.3 (5.4)	10
$FA_{0.8}Cs_{0.2}PbBr_3$	5.7 (6.4)	1.41 (1.45)	59 (65)	4.9 (5.8)	16

LiF/Al	I_{SC} / mA cm^{-2}	V_{OC} / V	FF / %	PCE / %	n
$FA_{0.8}Cs_{0.2}PbI_3$	16.4 (17.3)	1.02 (1.03)	57 (62)	9.6 (11.0)	14
$FA_{0.8}Cs_{0.2}Pb(I_{0.8}Br_{0.2})_3$	16.5 (17.2)	1.08 (1.10)	61 (66)	10.8 (12.1)	16
$FA_{0.8}Cs_{0.2}Pb(I_{0.6}Br_{0.4})_3$	9.5 (10.9)	1.14 (1.16)	64 (68)	8.5 (9.5)	7
$FA_{0.8}Cs_{0.2}Pb(I_{0.4}Br_{0.6})_3$	8.3 (9.7)	1.20 (1.21)	66 (72)	6.6 (7.7)	14
$FA_{0.8}Cs_{0.2}Pb(I_{0.2}Br_{0.8})_3$	5.5 (6.8)	1.10 (1.16)	60 (69)	3.7 (4.1)	10
$FA_{0.8}Cs_{0.2}PbBr_3$	4.9 (5.5)	1.33 (1.42)	67 (74)	4.4 (5.2)	23
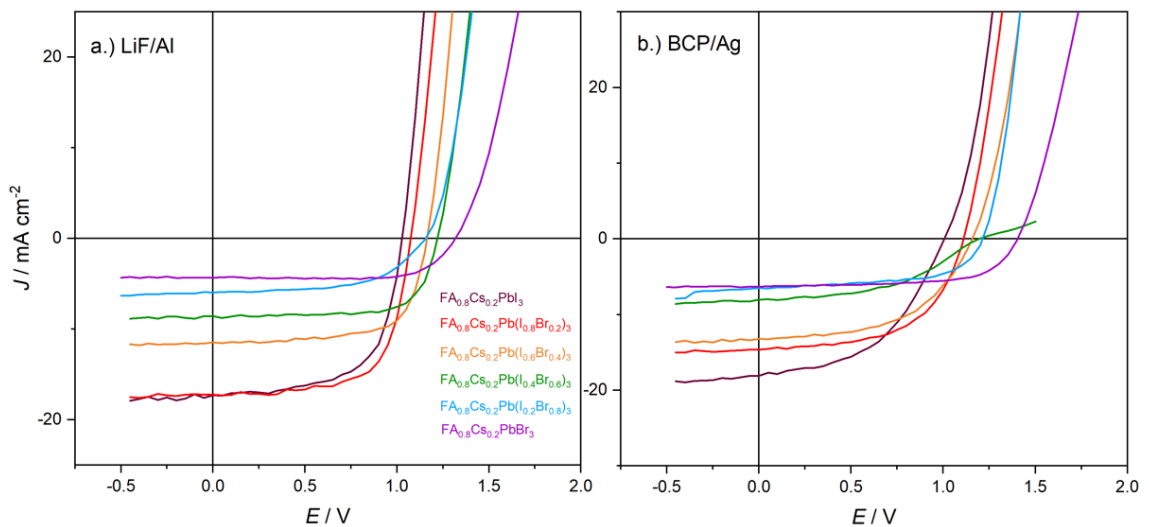
Figure 16: IV curves of the variations in the lead halide content. a.) depicts LiF/Al, whereas in b.) BCP/Ag is shown.

5.4   Influence of MeO-2PACz on the electrochemical band gap determination
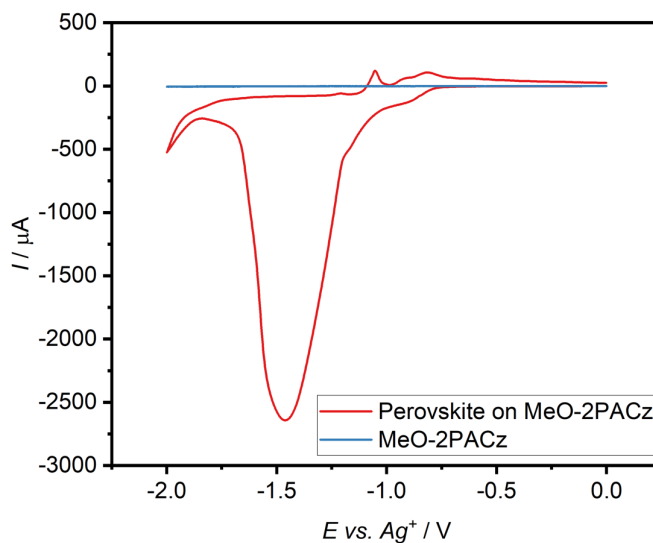
Figure 17: Influence of MeO-2PACz on the electrochemical band gap determination.

5.5   Optical evaluation method
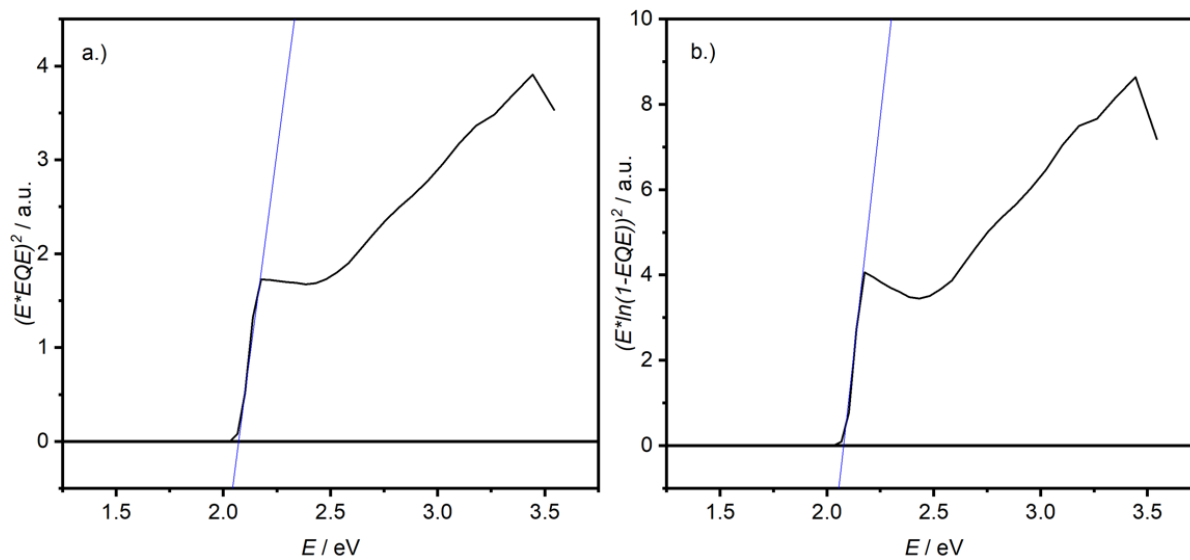
Figure 18: Integrated EQE curves. a.) shows the $(E \cdot EQE)^2$ method and b.) shows the $\ln^2(1 - EQE) \cdot E^2$ method.

5.6   Electrochemical evaluation method
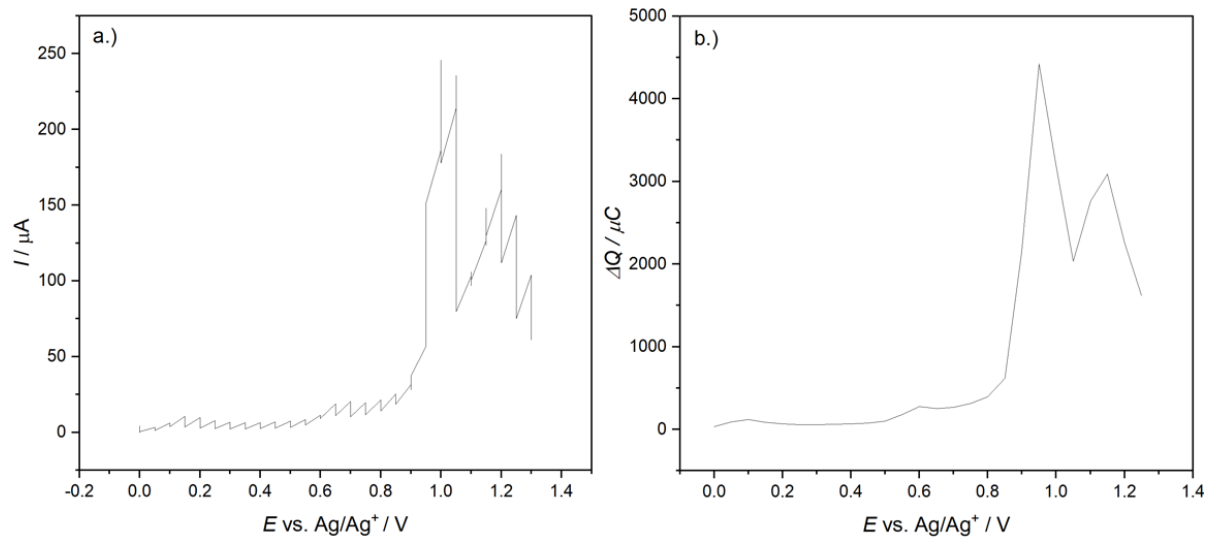
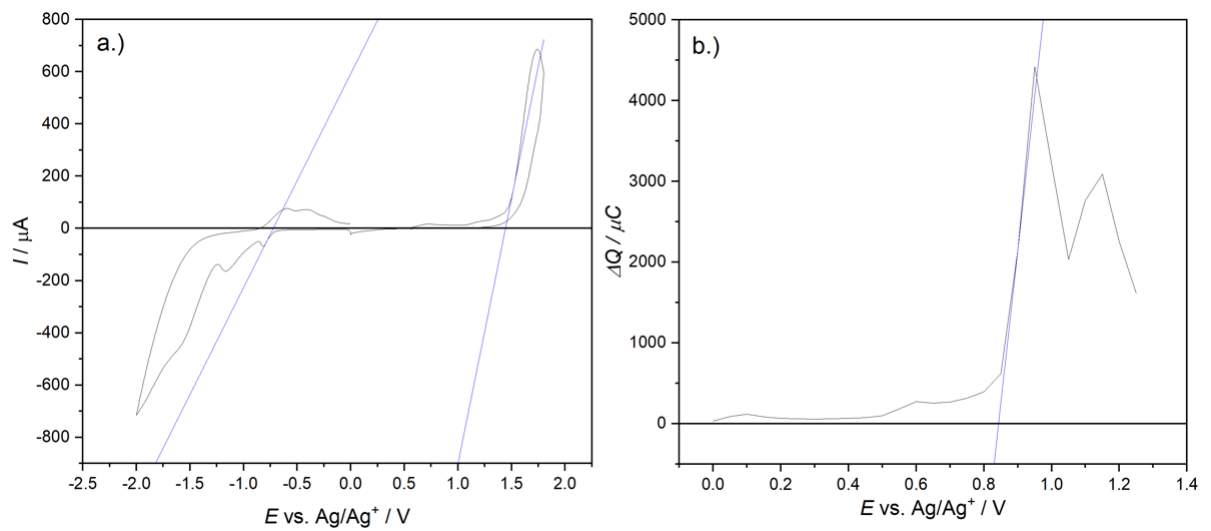**Figure 19:** Measured EVS curves. a.) shows the obtained raw data, whereas b.) shows the integrated form.

Figure 20: Evaluated CV (a.)) and EVS (b.)) graphs.

List of Figures

List of Tables

References

[1]   Z. H. Bakr, Q. Wali, A. Fakharuddin, L. Schmidt-Mende, T. M. Brown, R. Jose, *Advances in hole transport materials engineering for stable and efficient perovskite solar cells*, **2017**.

[2]   T. M. Koh, K. Fu, Y. Fang, S. Chen, T. C. Sum, N. Mathews, S. G. Mhaisalkar, P. P. Boix, T. Baikie, *Journal of Physical Chemistry C* **2014**, *118*, 16458–16462.

[3]   H. D. Kim, H. Ohkita, H. Benten, S. Ito, *Advanced Materials* **2016**, *28*, 917–922.

[4]   A. Al-Ashouri, A. Magomedov, M. Roß, M. Još, M. Talaikis, G. Chistiakova, T. Bertram, J. A. M. rquez, E. K. hnen, E. K. ius, S. Levcenco, L. Gil-Escrig, C. J. Hages, R. Schlatmann, B. Rech, dg Tadas Malinauskas, T. Unold, C. A. Kaufmann, L. Korte, G. Niaura, V. Getautis, S. Albrecht, *Energy Environ. Sci* **2019**, *12*, 3356.

[5]   R. Carron, C. Andres, E. Avancini, T. Feurer, S. Nishiwaki, S. Pisoni, F. Fu, M. Lingg, Y. E. Romanyuk, S. Buecheler, A. N. Tiwari, *Thin Solid Films* **2019**, *669*, 482–486.

[6]   G. F. Samu, R. A. Scheidt, P. V. Kamat, C. Janáky, *Chemistry of Materials* **2018**, *30*, 561–569.

[7]   P. Makuła, M. Pacia, W. Macyk, *The journal of physical chemistry letters* **2018**, *9*, 6814–6817.

[8]   J. Jimenez, J. Tomm, *Spectroscopic Analysis of Optoelectronic Semiconductors*, **2019**.

[9]   H. Kuzmany, *Springer Verlag Berlin Heidelberg* **2009**, *2*, 135.

[10] P. T. Kissinger, W. R. Heineman, *Cyclic voltammetry*, **1983**.

[11] J. Barker, Three electrochemical voltage spectroscopy (TECS): Evaluation of a model lithium ion system, **1995**, pp. 160–1608.

[12] C. M. Cardona, W. Li, A. E. Kaifer, D. Stockdale, G. C. Bazan, *Advanced Materials* **2011**, *23*, 2367–2371.

[13] C. Chen, Z. Song, C. Xiao, R. A. Awni, C. Yao, N. Shrestha, C. Li, S. S. Bista, Y. Zhang, L. Chen, R. J. Ellingson, C. S. Jiang, M. Al-Jassim, G. Fang, Y. Yan, *ACS Energy Letters* **2020**, *5*, 2560–2568.

[14] S. Yang, J. Dai, Z. Yu, Y. Shao, Y. Zhou, X. Xiao, X. C. Zeng, J. Huang, *Journal of the American Chemical Society* **2019**, *141*, 5781–5787.

[15] E. T. Hoke, D. J. Slotcavage, E. R. Dohner, A. R. Bowring, H. I. Karunadasa, M. D. McGehee, *Chemical Science* **2015**, *6*, 613–617.

[16] Y. Lin, A. Magomedov, Y. Firdaus, D. Kaltsas, A. El-Labban, H. Faber, D. R. Naphade, E. Yengel, X. Zheng, E. Yarali, N. Chaturvedi, K. Loganathan, D. Gkeka, S. H. AlShammari, O. M. Bakr, F. Laquai, L. Tsetseris, V. Getautis, T. D. Anthopoulos, *ChemSusChem* **2021**, *14*, 3569–3578.

[17] M. Giannouli, V. M. Drakonakis, A. Savva, P. Eleftheriou, G. Florides, S. A. Choulis, Methods for Improving the Lifetime Performance of Organic Photo-voltaicswith Low-Costing Encapsulation, **2015**, pp. 1–134.

[18] S. Ryu, J. H. Noh, N. J. Jeon, Y. C. Kim, W. S. Yang, J. Seo, S. I. Seok, *Energy and Environmental Science* **2014**, *7*, 2614–2618.

[19] S. Ameen, M. Abdulr, S. A. Kosa, K. A. Alamry,] M. S. Akhtar, H.-S. Shin, H.-K. Seo, A. M. Asiri, M. K. Nazeeruddin, Perovskite Solar Cells:Influence of Hole Transporting Materials on Power Conversion Efficiency, **2016**, pp. 10–27.